RSC Advances

ROYAL SOCIETY OF CHEMISTRY

PAPER

View Article Online
View Journal | View Issue

Check for updates

Cite this: *RSC Adv.*, 2025, **15**, 46164

Analytical evaluation of an Ag-MOF photocatalyst for efficient malachite green degradation in wastewater: kinetics, mechanism, and stability

Ahmed Hussain Jawhari *[a] and A. M. Ismael *[b]

Received 27th August 2025
Accepted 11th November 2025

DOI: 10.1039/d5ra06391d

rsc.li/rsc-advances

This work used a one-step solvothermal approach to construct a porous silver-based organic framework (Ag-MOF). The produced photocatalyst was thoroughly characterized using a variety of analytical methods, including FT-IR, UV-Vis, XRD, SEM, EDX, TEM, and BET analyses, to assess its surface morphology and crystal structure. According to DFT and UV-vis spectroscopic analyses, the bandgap energy of the Ag-MOF is around 2.9 eV. The influence of various experimental parameters such as the pH of the medium, dye concentration, amount of catalyst, and contact time for the degradation of the Malachite Green (MG) dye was examined. At optimum conditions (3 g L^{-1} of catalyst, pH 8, and 100 mg L^{-1} of the Malachite Green dye). The prepared Ag-MOF shows high photocatalytic activity of 97% at 90 min of reaction. Surface acidity investigations show that the total number of acid sites is 4.16 × 10^{26} acid sites per g. The preservation of more than half of the photocatalytic activity, even after 6 cycles of degradation, shows the stability and reusability of the prepared MOF. Comprehensive tests, including PL, TOC analysis, leaching studies, and pollutant degradation, were carried out to confirm the photocatalytic performance, mechanism, stability, and safety of the catalyst. Scavenging studies concluded that the inclusion of an $O_2^{\bullet-}$ scavenger significantly reduced the degradation efficiency to 31.12%. The study was extended to the use of the synthesized Ag-MOF for the synthesis of 7-hydroxy-4-methyl coumarin.

1. Introduction

Water contamination by synthetic dyes has emerged as an important environmental concern with significant consequences for aquatic life and human health due to their toxicity, persistence, and resistance to biodegradation.[1–3] Effluents from the textile, leather tanning, paper, and manufacturing sectors release huge quantities of dye-stained wastewater into water bodies, with malachite green (Fig. 1) being a regularly encountered cationic dye.[4] Of these sectors, the textile industry is the largest contributor to water pollution caused by dyes.

Malachite green (MG) dye is ecologically and environmentally problematic due to its toxicity. MG inhibits photosynthesis and is toxic to plant growth and development.[5,6] In aqueous media, MG is toxic to fish and other aquatic organisms, disrupts physiological processes, and compromises overall health.[7,8] Treatment of contaminated water is therefore essential for the preservation of the health and integrity of ecosystems as well as for the protection of public health.[9–11]

Therefore, affordable, simple, and environmentally friendly technologies for treating pollutants in water and wastewater need to be introduced. Of these, photocatalytic methods are a good choice, with benefits such as high efficiency, ease in operation, repeatability, and low price. This methodology offers a sustainable and effective way to face the drawbacks of conventional wastewater treatment processes, as it can achieve near-complete degradation of target pollutants without

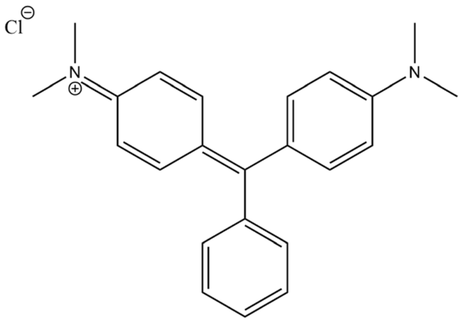

Fig. 1 Schematic diagram of Malachite Green (MG) dye. MG is primarily a cationic dye, specifically existing as a positively charged species due to its quaternary ammonium group, which significantly influences its adsorption behavior on photocatalysts like Ag-MOF. The chloride ion acts as the counter anion but does not affect the dye's chromophore.

---

[a] *Department of Physical Sciences, Chemistry Division, College of Science, Jazan University, P.O. Box. 114, Jazan 45142, Kingdom of Saudi Arabia. E-mail: Ahjawhari@jazanu.edu.sa*

[b] *College of Science, Mansoura University, Egypt. E-mail: Ismaelam11@hotmail.com*

producing harmful secondary by-products or catalyst residues during the reaction process.[12–15]

Over the past years, metal–organic frameworks (MOFs) have proven to be a promising group of catalytic materials for the treatment of wastewater. Their structural properties make them suitable for catalyzing many chemical reactions, such as the oxidation of organic contaminants.[16,17] One of the principal advantages of MOFs in environmental use is their structural flexibility and tunability, which can enable MOFs to be functionalized and tailored to have distinctive catalytic capacities for efficient degradation of most organic pollutants.[17–19]

Silver (Ag) was selected as the metal node for MOF synthesis due to its unique physicochemical properties that directly enhance photocatalytic performance. Ag-containing MOFs have demonstrated broad-spectrum light absorption, strong surface plasmon resonance, and efficient charge separation capabilities, resulting in superior visible-light-driven photocatalytic activity compared to conventional MOFs. Additionally, Ag imparts high electrical conductivity, which facilitates the rapid transport of photoinduced charge carriers and suppresses electron–hole recombination, further boosting photocatalytic degradation rates for various pollutants.[20–22]

The combination of Ag with organic linkers within the MOF architecture provides a highly porous and tunable platform, enabling optimal adsorption and interaction with target contaminants. Recent studies have shown that Ag-MOFs not only possess high chemical stability and reusability, but also outperform pure MOFs or metal oxides in photocatalytic applications, particularly in the degradation of organic dyes and industrial pollutants.[23,24]

In this study, a silver-based MOF was prepared by the green solvothermal method. Various techniques such as FTIR, UV-Vis, PXRD, SEM, EDX, TEM, and BET were used to characterize the nanocomposite. The photoactivity of the Ag-MOF toward MG dye degradation was assessed. The study investigated the optimization of extraneous parameters. Additionally, the use of the Ag-MOF catalyst in the synthesis of 7-hydroxy-4-methyl coumarin was investigated.

2. Experimental

2.1. Materials

The used chemicals, such as silver acetate, organic linker niacin (nicotinic acid or vitamin B_3) and other solvents, were purchased from Sigma Aldrich. The following methods and techniques were used to characterize the synthesized Ag-MOF. UV/Vis spectra were recorded using a PG UV/Vis spectrometer T80+. Powder X-ray diffraction (PXRD) patterns were obtained with Ni-filtered Cu Kα radiation ($\lambda = 1.540$ Å) at 40 kV and 30 mA, over a scanning range of $2\theta = 3°–70°$. PXRD indexing was performed using preDICT software with DICVOL14.[25] Fourier-transform infrared (FTIR) spectra were recorded from 4000–400 cm^{-1} using a Thermo Scientific Nicolet iS10 FT-IR Spectrometer. Scanning electron microscopy (SEM) and energy-dispersive X-ray (EDX) analyses were conducted using a JEOL JSM-6510 microscope. Transmission electron microscopy (TEM) images were acquired with a JEOL JEM-2100 plus. Frontier molecular orbitals (FMOs), including HOMO and LUMO, were calculated using the B3LYP/LANL2DZ method in Gaussian 09 (G09), with visualization performed *via* GaussView 6.0 and Multiwfn.[26–28]

2.2. Synthesis of Ag-MOF

0.246 g Niacin was dissolved in 30 mL DI water and 10 mL ethylene glycol solution and stirred at 90 °C for 30 minutes. 0.334 g Silver acetate was dissolved in the same solvent mixture in another reactor and added to the solution of niacin under stirring at 60 °C. The mixture was then placed in a 100 mL Teflon-lined autoclave and heat-treated at 90 °C for 36 hours. The precipitate was then taken, washed in warm deionized water (50 °C) *via* centrifugation at 7000 rpm, and dried at 90 °C for 6 hours.[29]

2.3. Photodegradation activity

2.3.1. Ag-MOF photodegradation activity against malachite green (MG). In a 100 mL Erlenmeyer flask, 0.05 g of Ag-MOF was combined with 50 mL of MG solution in water (100 ppm). To ensure the Ag-MOF was dispersed and to ensure the adsorption/desorption equilibrium, the solution was stirred in the dark before the UV lamp (10 W high-pressure Hg lamp with 254 nm mean wavelength inside a cylindrical reactor with 27 cm length and 2.5 cm diameter) was switched on. Finally, the mixture was centrifuged, and the Ag-MOF was removed. 1 mL of dye solution was diluted to 10 mL using distilled water. The spectrophotometer was set to monitor the maximum MG wavelength of 617 nm, and concentrations were recorded every 10 minutes. The dye decolorization was calculated as follows: degradation (%) $= (C_o - C_t)/C_o \times 100$, where C_t is the concentration at time t and C_0 is the initial concentration of each solution. Control experiments were conducted to isolate the effects of adsorption and photolysis. For adsorption controls, 0.15 g Ag-MOF was dispersed in 50 mL of 100 mg per L MG solution at pH 8 and stirred in the dark for 120 minutes. Samples were withdrawn at intervals, centrifuged, and analyzed *via* UV-Vis spectroscopy at 617 nm to calculate removal percentage using the formula: removal (%) $= (C_0 - C_t)/C_0 \times 100$, where C_0 is the initial concentration and C_t is the concentration at time t. For photolysis controls, the same MG solution was irradiated under UV light (10 W Hg lamp, 254 nm) without Ag-MOF for 120 minutes, with sampling and analysis as above.

2.3.2. Mineralization assessment *via* TOC analysis. To evaluate the extent of mineralization during the photocatalytic degradation of malachite green (MG), total organic carbon (TOC) measurements were performed. MG aqueous solutions were sampled before and after photocatalytic treatment under the optimized conditions. All samples were filtered to remove the catalyst and analyzed for TOC content using a Shimadzu TOC-L analyzer. The mineralization efficiency was calculated by: % TOC removal $= ((\text{TOC}_\text{i} - \text{TOC}_\text{f})/\text{TOC}_\text{i}) \times 100$.

2.3.3. Photocatalytic degradation of additional organic pollutants. To further evaluate the versatility of the Ag-MOF photocatalyst, its efficacy against a range of environmentally relevant organic contaminants, including tetracycline,

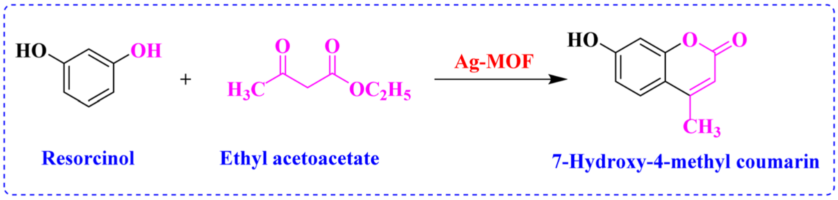

Scheme 1 Synthesis of 7-hydroxy-4-methyl coumarin.

norfloxacin, acetaminophen, and atrazine, was investigated. Each pollutant aqueous solution (20 mg L^{-1}) was subjected to photocatalytic treatment under the optimized conditions.

2.4. Synthesis of 7-hydroxy-4-methyl coumarin

Using the Ag-MOF catalyst, resorcinol and ethyl acetoacetate underwent Pechmann condensation to form a coumarin derivative (Scheme 1).[30] To generate 7-hydroxy-4-methyl coumarin, 2.2 g of resorcinol and 5 mL of ethyl acetoacetate (EAA) were mixed in a 50 mL round-bottomed flask. The solution was then supplemented with 0.1 g of Ag-MOF that had been activated for two hours at 120 °C. The flask was refluxed at 120 °C in an oil bath for two hours, and TLC was used to trace the reaction until completion. After filtration, the resulting liquid was transferred to a beaker filled with crushed ice. The product's melting point (185 °C) was utilized to confirm its identity and purity.[31,32] The following formula was used to determine the yield of the 7-hydroxy-4-methyl coumarin: yield % = (obtained wt of product ÷ theoretical wt of product) × 100.

3. Results and discussions

3.1. FTIR

The FT-IR spectra of the niacin linker and Ag-MOF are shown in Fig. 2. The characteristic signals at 1743, 1640, and 1533 cm^{-1} are due to the C═O, C═C, and C═N stretching, respectively. The weak band at 3120 cm^{-1} is characteristic of C–H, which is weakened by conjugation and the presence of the COOH group, which reduces the dipole moment during vibration, resulting in a weaker C–H stretch. Bands at 1462, 1342 and 1077 cm^{-1} are attributed to C–H bending and C–N and C–O stretching, respectively. The broad band at 2470 cm^{-1} is related to a hydrogen-bonded O–H stretching of the –COOH group, which appears at a lower wavenumber due to hydrogen bonding and electronic effects from the surrounding functional groups. In the Ag-MOF spectrum, the disappearance of the broad band at 2450 cm^{-1} indicates that the carboxyl group is no longer hydrogen-bonded due to the formation of a metal-carboxylate bond in which the carboxyl group is coordinated to Ag. The shift of the carbonyl bands to 1723 cm^{-1} indicates that the carboxylate group is now coordinated to the silver metal. The ring stretching frequencies of pyridine (1575 and 1502 cm^{-1}) indicate possible interactions between Ag and the nitrogen of pyridine. These shifts reflect the structural modifications occurring upon the inclusion of niacin in the Ag-niacin MOF.

3.2. XRD analysis

The crystallinity and purity of the synthesized Ag-MOF were investigated using PXRD, as shown in Fig. 3. The diffraction pattern exhibits a series of sharp and intense peaks over the 2θ

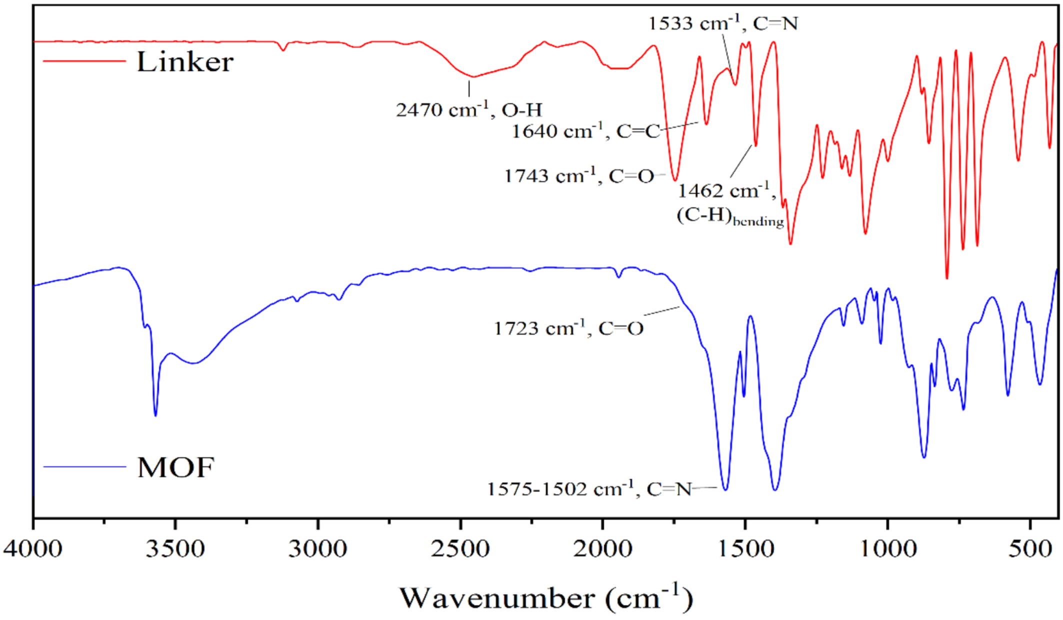

Fig. 2 IR spectra of the niacin linker and the Ag-MOF.

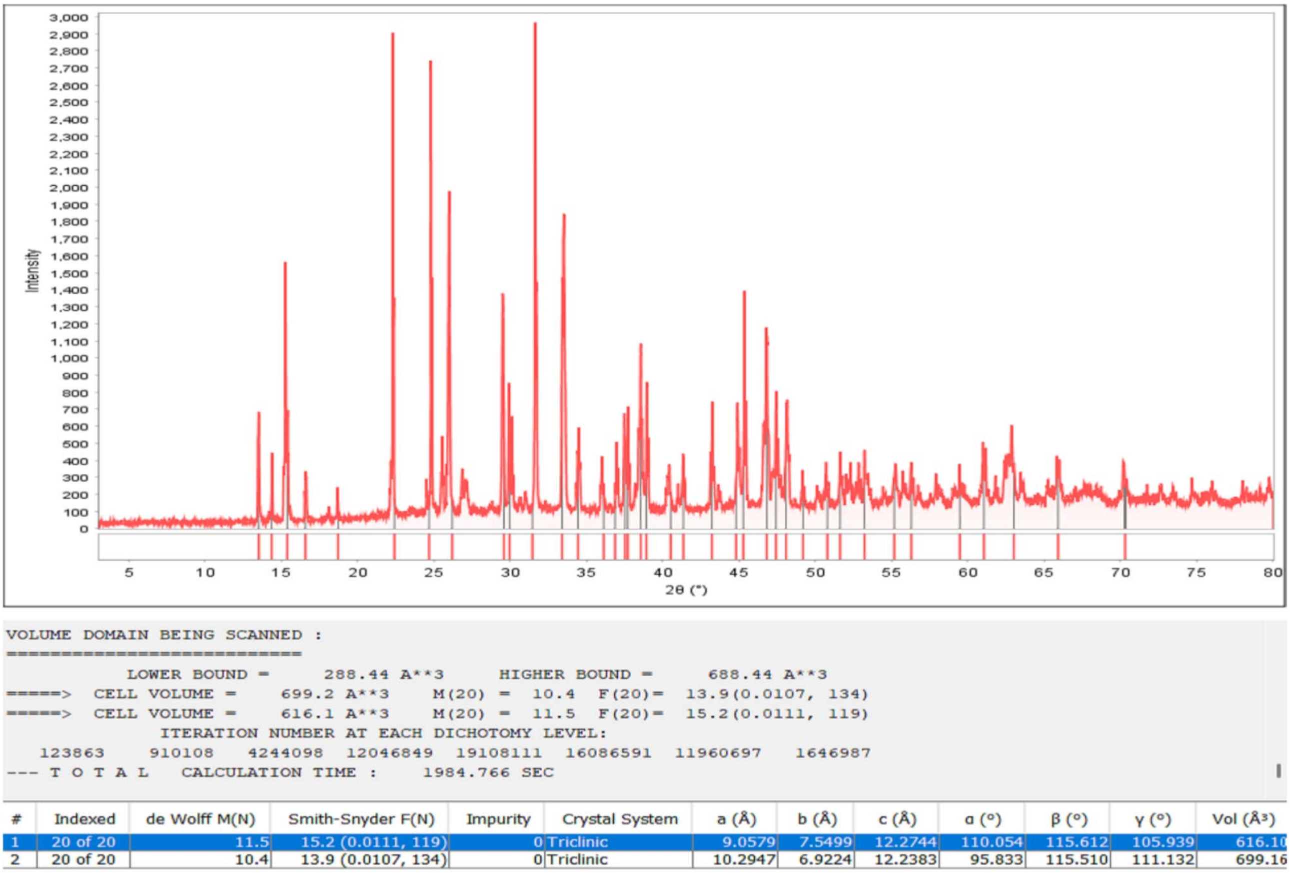

```
VOLUME DOMAIN BEING SCANNED :
===============================
               LOWER BOUND =      288.44 A**3      HIGHER BOUND =      688.44 A**3
=====>  CELL VOLUME =     699.2 A**3     M(20)  =  10.4   F(20)=  13.9(0.0107, 134)
=====>  CELL VOLUME =     616.1 A**3     M(20)  =  11.5   F(20)=  15.2(0.0111, 119)
                 ITERATION NUMBER AT EACH DICHOTOMY LEVEL:
   123863     910108    4244098   12046849   19108111   16086591   11960697    1646987
--- T O T A L    CALCULATION TIME :     1984.766 SEC
```

#	Indexed	de Wolff M(N)	Smith-Snyder F(N)	Impurity	Crystal System	a (Å)	b (Å)	c (Å)	α (°)	β (°)	γ (°)	Vol (Å³)
1	20 of 20	11.5	15.2 (0.0111, 119)	0	Triclinic	9.0579	7.5499	12.2744	110.054	115.612	105.939	616.10
2	20 of 20	10.4	13.9 (0.0107, 134)	0	Triclinic	10.2947	6.9224	12.2383	95.833	115.510	111.132	699.16

Fig. 3 PXRD pattern of the Ag-MOF with the output obtained from preDICT.

range of 5° to 80°. The PXRD pattern matches well with the simulated diffraction data, thereby confirming the phase purity of the synthesized Ag-MOF material. The PXRD pattern of the Ag-MOF was also examined by indexing using the preDICT software with DICVOL14. The most probable indexing solutions are for a triclinic unit cell, with two almost identical sets of parameters discovered. The best fit ($M(20) = 11.5$, $F(20) = 15.2$) provided lattice parameters a = 9.0579 Å, b = 7.5499 Å, c = 12.2744 Å, and angles $\alpha = 110.05°$, $\beta = 115.61°$, and $\gamma = 105.94°$, with a cell volume of 616.1 Å^3. The cell is consistent with the diffraction pattern seen, confirming the single-phase material (0% impurity).

3.3. Morphological analysis

A silver-based 3D metal–organic framework using niacin as the organic linker was synthesized (Fig. S1). This MOF features silver nodes coordinated to nitrogen and oxygen atoms of niacin molecules, forming a porous network conducive to photocatalytic degradation. The structure resembles typical MOFs constructed from monovalent metals and nitrogen-containing organic ligands, classified as coordination polymers, resulting in enhanced photocatalytic performance. The SEM images of the sample are shown in Fig. 4. The Ag-MOF crystals exhibited irregular polyhedral morphology with faceted crystalline structures, with particles ranging from approximately 0.5 to 3 µm exhibiting a rough and porous surface. In Fig. 4, the EDX elemental map images of the prepared materials show uniform elemental distributions of C, N, O, and Ag, further verifying that the synthesized MOF material is composed of the expected elements.

The TEM image (Fig. 4) shows the diverse sizes of the Ag-MOF particles, from 26 to 52 nm, which exhibit moderate agglomeration and a polycrystalline or partially amorphous structure. Based on the SEM and TEM images, the Ag-MOF appears to have promising features for use in the photodegradation of dyes.

3.4. Thermal analysis

The thermal stability of the synthesized Ag-MOF was evaluated using thermogravimetric analysis (TGA) and its derivative (DrTGA), as illustrated in Fig. 5. The TGA curve reveals a multi-step decomposition process. The first weight loss of 6.74%, occurring below 200 °C, is attributed to the evaporation of physically adsorbed water molecules and possibly residual solvents confined within the MOF's structure. The subsequent and more significant weight loss of 21.63% is observed between 200 °C and 400 °C, corresponding mainly to the removal of coordinated organic ligands and some partial disruption of the framework itself.

As the temperature increases from 400 °C to 600 °C, a further weight loss of 26.35% is recorded, which is associated with the decomposition of the major organic components integral to the

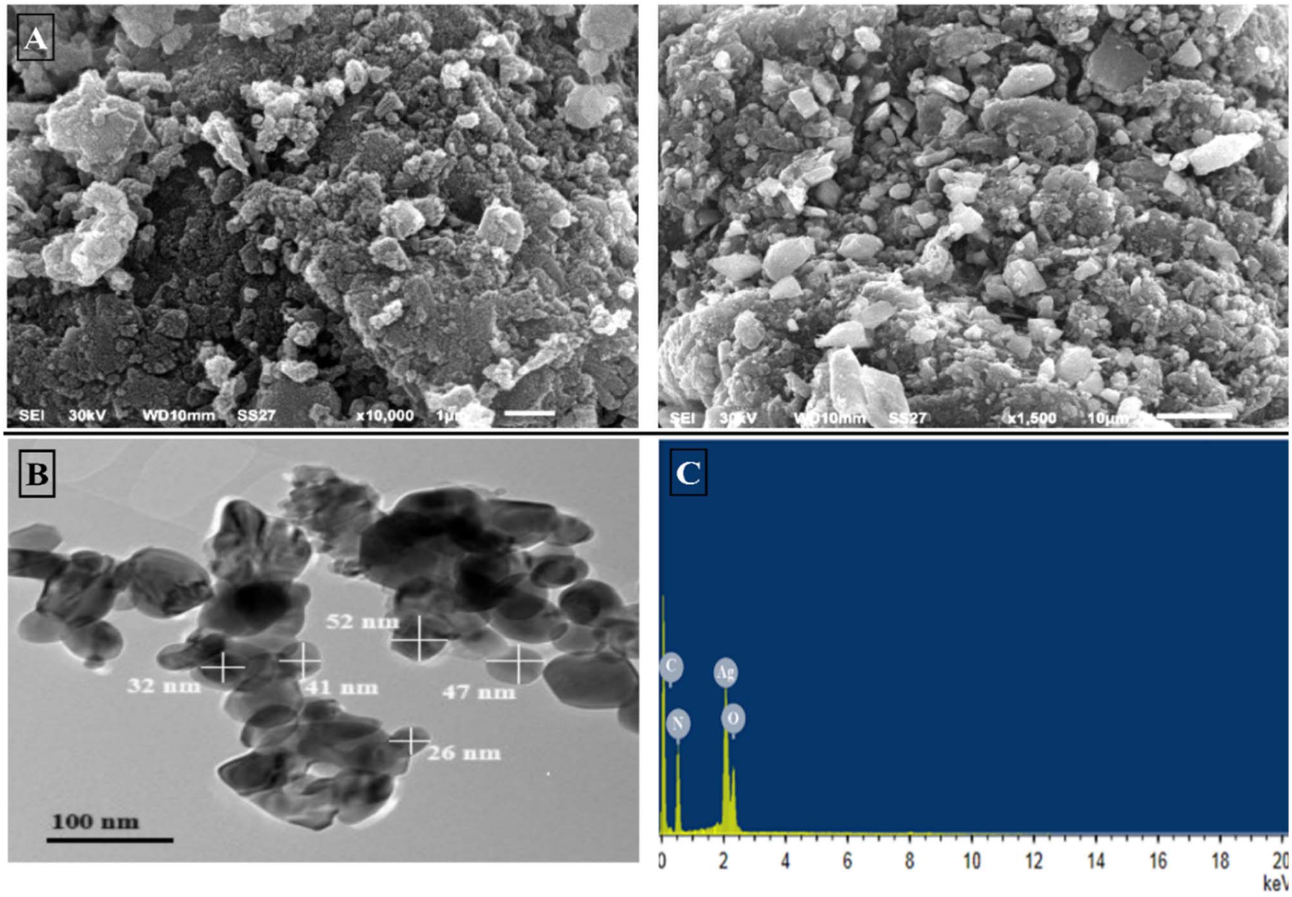

Fig. 4 (A) SEM and (B) TEM images, and (C) the EDX spectrum of Ag-MOF.

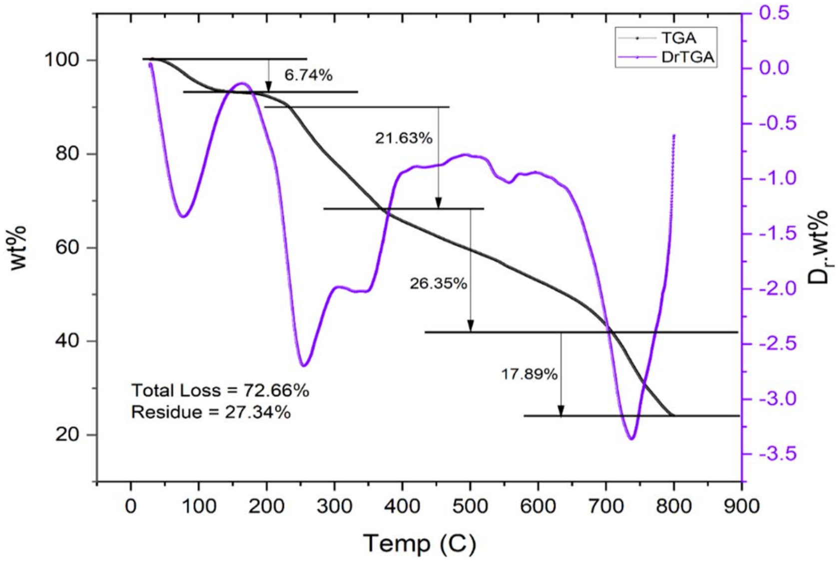

Fig. 5 TGA and DrTGA plots of Ag-MOF.

MOF backbone, leading to substantial framework collapse. In the range of 600 °C to 750 °C, an additional weight loss of 17.89% takes place, signifying the ultimate breakdown of persistent organic residues and transformation toward an inorganic phase. By the end of the analysis at 800 °C, the Ag-MOF retains a residue of 27.34% of its original mass, reflecting a high metal (inorganic) content and a total weight loss of 72.66%. The DrTGA curve further corroborates these decomposition stages, showing distinct peaks at the temperatures corresponding to the main weight-loss steps. Collectively, these results attest to the good thermal stability of the Ag-MOF up to approximately 200 °C and detail its characteristic multistage thermal decomposition profile.

3.5. Photoelectronic properties

The optoelectronic properties of the Ag-MOF were investigated using UV-Vis spectroscopy. As seen in Fig. 6, the MOF exhibits intense UV absorption, particularly from 200 to 400 nm, with the absorption edge occurring at around 420 nm. The absorption decreases gradually beyond 450 nm, suggesting little interaction with visible light. To obtain more information on the electronic structure, the optical band gap was estimated using a Tauc plot,[33] and by extrapolating the linear section of the plot to the energy axis, the band gap energy was determined to be *ca.* 2.95 eV. Such a moderate band gap enables the MOF to generate electron–hole pairs under UV light, favoring its utilization for photocatalytic degradation of organic dyes.[34]

To gain insight into the charge carrier behavior of the MOF photocatalyst, we measured its photoluminescence (PL) spectrum at room temperature (Fig. 6). The resulting spectrum exhibits a broad emission profile that rapidly decreases in intensity beyond the initial region, followed by smaller undulating peaks and an overall plateau at longer wavelengths. This relatively weak PL response suggests that photogenerated electrons and holes in the MOF are effectively separated and less prone to recombine radiatively. This implies that more charges are available to migrate to the surface of the photocatalyst, where they can participate in the redox reactions that generate the reactive species responsible for pollutant degradation.

3.6. BET study

As can be seen in Fig. 7, the BET plot of the MOF can be classified as a type-IV isotherm, characterized by a distinct hysteresis loop between the adsorption (black) and desorption (red) branches, indicating the presence of meso-porosity. The BJH pore size distribution curve of the Ag-MOF (Fig. 7) reveals a prominent peak in the range of 2 to 10 nm, indicating that the material predominantly possesses mesoporous characteristics. The sharp drop in intensity beyond this range shows the smaller contribution of larger mesopores or macropores. The occurrence of other small peaks in the range from 15 to 30 nm points to a broader pore size distribution but with very low intensity, further supporting the hierarchical mesoporous nature of the material. The BET surface area of the synthesized Ag-MOF was measured to be approximately 97.6 $m^2\ g^{-1}$, indicating high porosity, which supports significant dye adsorption during the dark phase before UV irradiation. Therefore, the Ag-MOF is endowed with favorable surface properties, including high surface area and mesoporous structure, which enable easy diffusion of reactants and exposure of active sites.

3.6.1. Acidity.

The number of Ag-MOF surface acid sites was measured using potentiometric titration. By adding *n*-butylamine, the surface acid sites were neutralized, and the electrode potential (mV) was monitored in response to the increasing *n*-butylamine concentration (mmol per g catalyst).[35] The following formula was used to compute the total number of acid sites: total number of acid sites per g = (mL equivalent per g) × $N \times 10^3$, where N is Avogadro's number. The total number of acid sites in Ag-MOF was found to be 4.16×10^{26} acid sites per g (Fig. 8).

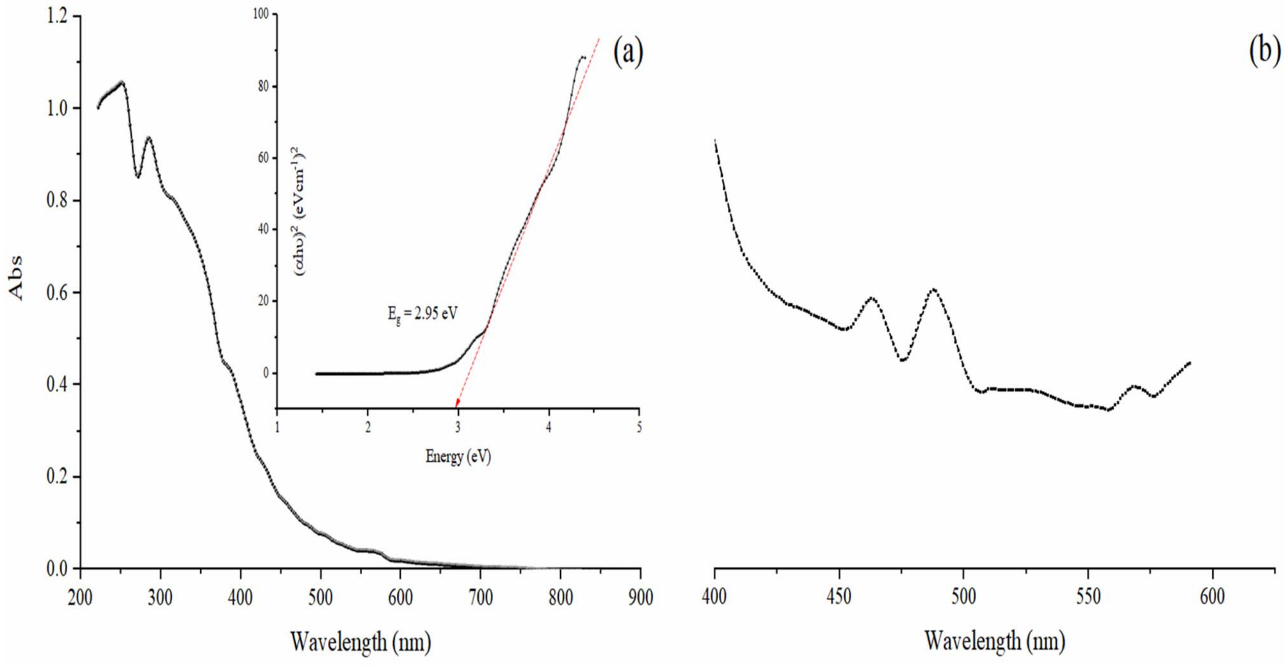

Fig. 6 (a) UV-Vis spectrum, Tauc plot, and (b) PL spectrum of Ag-MOF.

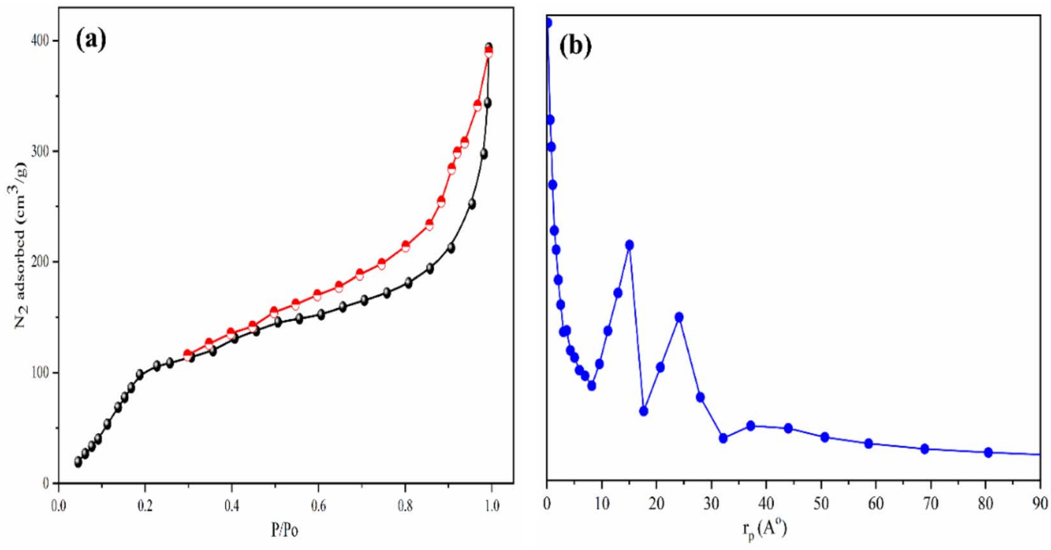

Fig. 7 (a) BET plot and (b) BJH pore size distribution curve of Ag-MOF.

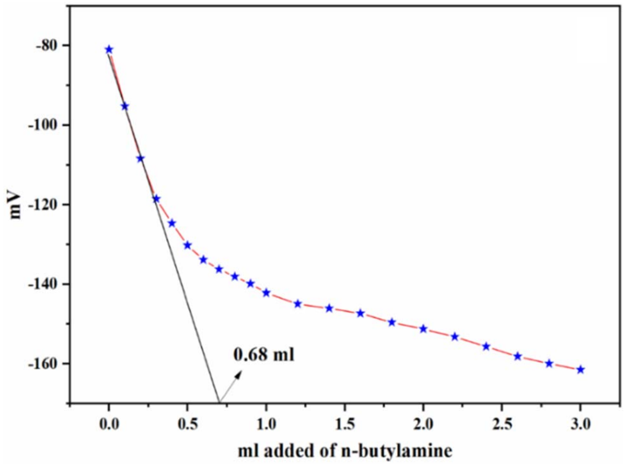

Fig. 8 Potentiometric titration acidity curve of Ag-MOF.

3.7. Computational study

The electronic structure of the Ag-MOF was further studied by DFT calculations to explore its photocatalytic behavior. The calculated energy levels show HOMO and LUMO values of −6.146 and −3.247 eV, respectively, leading to a theoretical E_g of 2.898 eV. This value is in good agreement with the experimentally obtained optical band gap from the Tauc plot (2.95 eV). The close match indicates the reliability of the DFT calculations (Fig. S2). The HOMO–LUMO separation suggests good electron–hole separation, which is good for photocatalytic processes. Ionization potential (I; energy to remove an e^-) and electron affinity (A; energy on gaining e^-) were calculated to be 6.146 and 3.247 eV, respectively, and the electronegativity was calculated to be 4.697 eV ($\chi = (I + A)/2$). Chemical hardness (η), $(I - A)/2$, and electrophilicity index (ω), $\chi^2/2\eta$, were calculated to be 1.449 and 7.611 eV, respectively.[36,37] These are in line with moderate resistance against CT and the capacity for accepting electrons in redox processes. Hardness combined with electrophilicity is at the origin of control over charge recombination as well as the enhancement of interactions between molecules of the dye, which are both requirements for efficient photocatalysis.

3.8. Photocatalytic degradation of malachite green dye

The synthesized Ag-MOF has a band gap of about 2.95 eV, which means it mainly absorbs UV light. Therefore, we used a 10 W high-pressure mercury lamp emitting UV light at 254 nm to drive the photocatalytic degradation of Malachite Green. This UV light provides enough energy to excite electrons in the catalyst, creating reactive species that break down the dye. Although the material shows some absorption in the visible range due to silver's plasmon resonance, the main photocatalytic activity relies on UV excitation. The Ag-MOF we synthesized in this study was investigated for its activity as a photocatalyst for the photodegradation of MG dye, which is present in industrial effluent and recovered for use in agriculture. The degradation of the dye after 90 minutes of UV irradiation achieved a maximum of 97%, according to the Ag-MOF's photocatalytic data. Various effects were investigated, including the solution pH, time of irradiation, dosage of Ag-MOF, and initial concentration of MG, in addition to assessing the sustainability and reusability of the Ag-MOF. Mass transfer limitations were minimized by continuous stirring at 300 rpm, ensuring uniform Ag-MOF dispersion and MG diffusion, with no constraints evident from the rapid initial rates and the kinetic profile's lack of diffusion plateaus. Light transfer was assessed *via* dosage optimization, showing peak efficiency at 0.15 g/50 mL with a decline at higher loadings due to turbidity-induced scattering. Beer–Lambert estimates confirmed sufficient ~2–3 cm penetration in our reactor. Under the optimized conditions, these limitations are negligible, allowing photocatalysis to be governed by intrinsic kinetics.

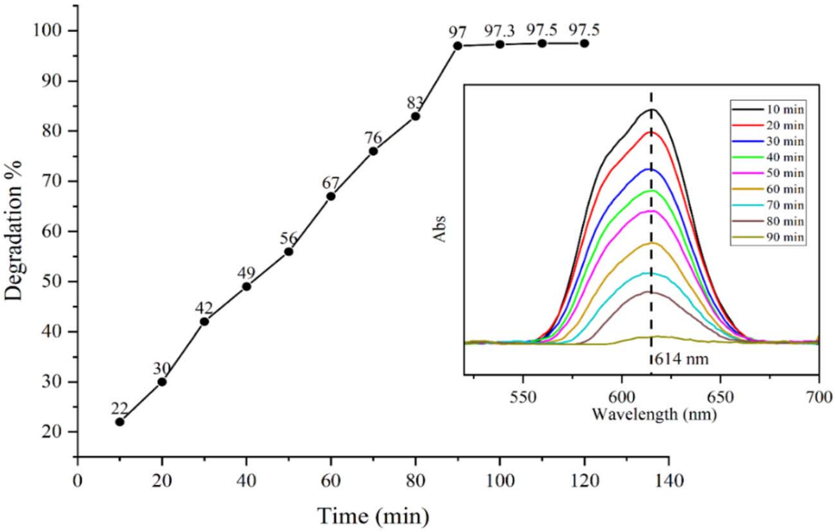

Fig. 9 Time of irradiation effect on the degradation of MG dye and time-dependent UV-Vis spectra for degradation over 90 min.

3.8.1. Time of irradiation. Both adsorption on the Ag-MOF during the dark phase and photocatalytic degradation under UV light were studied to measure dye uptake before irradiation. The influence of irradiation time on photocatalytic degradation efficiency was systematically evaluated over a range of 10 to 120 minutes (Fig. 9). As depicted, the percentage of dye removal increased consistently with longer irradiation periods, rising sharply from approximately 20% at 10 minutes to over 97% at 90 minutes. The time-dependent UV-Vis spectra show a rapid decrease in the main absorbance peak at 614 nm, evidencing efficient photocatalytic degradation and color removal from the solution. Beyond this point, the degradation rate plateaued, with only marginal increases observed up to 120 minutes. This trend indicates that prolonged exposure enhances dye breakdown up to a threshold, after which the photocatalyst approaches its maximum removal capacity. The rapid initial rise is attributed to abundant active sites and high pollutant concentration, facilitating efficient generation of reactive species. The subsequent plateau suggests that, as the dye concentration diminishes, the reaction moves toward completion and becomes limited by factors such as the reduced availability of target molecules or the saturation of active sites.

3.8.2. Solution pH. As demonstrated in Fig. 10, the pH has a considerable influence on the rate of MG decolorization. It affects the stability of the adsorbate solution as well as the intensity of its color. As a result, one of the most critical parameters affecting the adsorption process is pH. In order to identify the appropriate pH of the solution, the adsorption of MG dye on the surface of Ag-MOF was examined at various pH values ranging from 2 to 12 with a fixed starting dye concentration of 100 ppm and a contact period of 90 min. The figure depicts how the dye removal efficiency grows in line with the solution pH, peaking at approximately 8 and then decreasing to the lowest efficiency. Due to a drop in surface charge density and an increase in electrostatic attraction between the MOF and

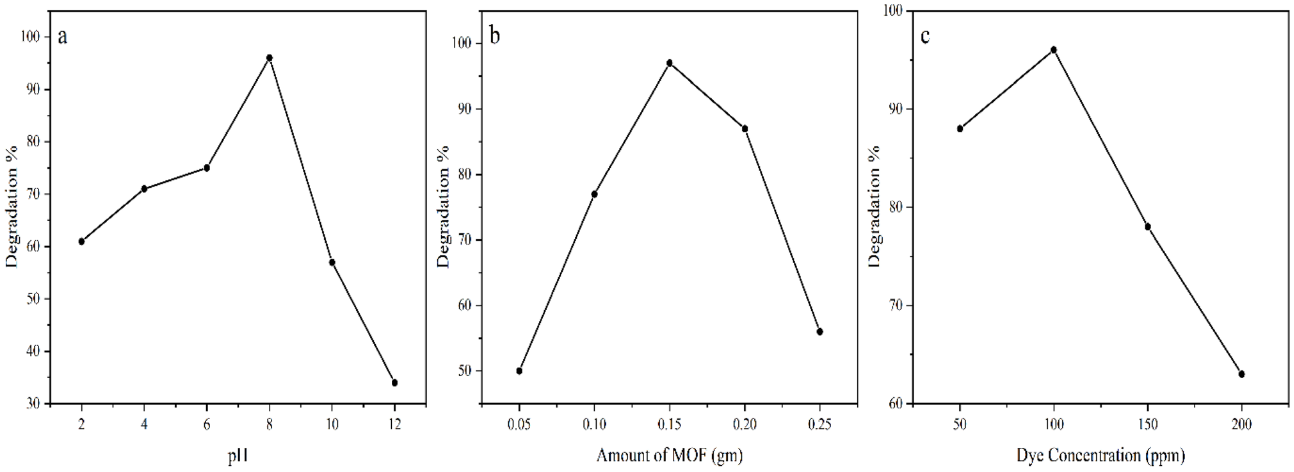

Fig. 10 Effects of (a) solution pH, (b) dosage of Ag-MOF, and (c) initial MG concentration.

the MG dye at a pH of about 8, the percentage of adsorption increases to 96%.

3.8.3. Dosage of Ag-MOF. The photocatalytic degradation of MG was studied by increasing the photocatalyst dosage from 1 to 5 g L^{-1}. The results demonstrate that the degrading efficiency is enhanced by increasing the photocatalyst weight up to 0.15 g, as illustrated in Fig. 10. A possible explanation can be that a high concentration of the photocatalyst (above 0.15 g) makes the solution more turbid, which obstructs and filters the irradiation light and causes it to diffuse in particular locations, lowering the photocatalytic efficacy.

3.8.4. Initial MG concentration. Fig. 10 demonstrates the photocatalytic activity of a range of starting concentrations of MG dye. It was found that the photodegradation rate increased to nearly 96% when the original dye concentration was increased to 100 ppm. Following that, it gradually declined when the initial concentration was elevated to 200 ppm. This could be because the dye absorbs light photons, lowering the number of photons needed to synthesize OH$^{\bullet}$. However, the active sites are accessible at low concentrations, and the photocatalytic activity is improved by boosting the dye concentration to the ideal level of 100 ppm.

3.8.5. Kinetic study. To better understand how efficiently the Ag-MOF catalyst removes MG, we tracked how much dye was left in the solution at different times during the photocatalytic reaction. With these measurements, we calculated the fraction of dye remaining (C_t/C_o) and then applied a pseudo-first-order kinetic model, which is commonly used for these types of systems. The relation between $\ln(C_o/C_t)$ and time was plotted to determine how well the reaction fits this model. As shown in Fig. 12, dye removal increased rapidly at first and then leveled off as the reaction approached completion.

The mean values with standard deviations are presented as error bars in Fig. S3. Adsorption and photolysis controls exhibited low removal efficiencies, plateauing at 13% and 6% respectively, each with a standard deviation consistently below 1.2%. In contrast, the photocatalytic process demonstrated rapid and efficient degradation, achieving 97% removal at 90 minutes with a maximum standard deviation of 5.4%. Kinetic modeling of the photocatalytic data yielded a pseudo-first-order rate constant of $k = 0.0301$ min^{-1} and an excellent fit ($R^2 = 0.9918$). The Absolute Relative Error (ARE) for our kinetic model fitting gave an ARE value of approximately 12.0%. This, alongside a high R^2 value, demonstrates a reasonable and robust fit quality for the degradation kinetics.

The concentration-dependent uptake kinetics were evaluated through $q(t)$ profiles, calculated as $q(t) = [(C_o - C_t) \times V/m]$ (where $V = 0.05$ L, $m = 0.15$ g, pH 8). For initial malachite green concentrations of 50–200 mg L^{-1}, $q(t)$ shows rapid initial uptake (0.5–0.8 mg g^{-1} min^{-1}) reaching equilibrium by ∼100 min, with maximum capacities increasing to 58.5 mg g^{-1} at 150 mg L^{-1} before declining to 39.7 mg g^{-1} at 200 mg L^{-1} due to active site saturation and photon competition, despite lower % degradation at higher C_o (Fig. S4). The results confirm the optimal absolute uptake near 150 mg L^{-1} and align with the pseudo-first-order kinetics ($k = 0.0301$ min^{-1}, $R^2 = 0.99$) and Langmuir isotherm saturation.

3.8.6. Optimization of photocatalytic parameters. To address the influence of operational variables on photocatalytic degradation efficiency, systematic single-factor experiments were conducted in triplicate, evaluating the main effects of catalyst dosage, initial malachite green (MG) concentration, and pH while keeping other parameters constant (irradiation time: 90 min, volume: 50 mL). Catalyst dosage showed a pronounced main effect, with mean efficiency increasing from 50% ± 0.82% at 0.05 g to 76% ± 2.83% at 0.10 g. Efficiency reached its maximum value of 97% ± 2.45% at 0.15 g, before slightly declining to 86% ± 1.41% at 0.20 g, likely due to agglomeration and light scattering that reduced active site accessibility. Initial MG concentration exhibited an inverse main effect, peaking at 95.6% ± 1.7% for 100 mg L^{-1} and dropping to 75% ± 3.6% at 150 mg L^{-1}, attributable to increased light attenuation and competition for reactive species at higher loads; pH displayed a bell-shaped response, achieving maximum efficiency of 96.3% ± 1.2% at pH 8 (favorable for electrostatic attraction between cationic MG and the Ag-MOF surface), compared to 75.0% ± 1.7% at pH 6 and 56.0% ± 1.2% at pH 10. These main effects, summarized in Table S1, confirm the optimized conditions reported (0.15 g catalyst, 100 mg per L MG, pH 8) and align with pseudo-first-order kinetics (rate constant: 0.0301 min^{-1}).

3.8.7. Mechanism of degradation. The photocatalytic mechanism for malachite green decomposition is influenced by the Ag-MOF surface charge, with the point of zero charge (pH$_{\text{pzc}}$) determined as ≈5.2 *via* zeta potential measurements in 0.01 M NaCl (Fig. 11). At the optimal experimental pH 8 (>pH$_{\text{pzc}}$), the surface exhibits a negative zeta potential ($\zeta \approx -25$ mV), facilitating electrostatic attraction and adsorption of cationic dye (q_e up to 58.5 mg g^{-1}), which enhances the proximity for photogenerated holes and OH radicals and drives oxidation, decolorization, and mineralization.

3.8.8. Photocatalytic decomposition isotherms. The photocatalytic isotherms were derived from UV-Vis measurements of MG concentrations (50–200 mg per L initial), with fixed conditions (0.15 g catalyst, pH 8, 120 min irradiation) (Table S2). The equilibrium capacity q_e was calculated to be 22.0–63.0 mg g^{-1}. Non-linear fits gave Langmuir parameters $q_m = 52.6$ mg g^{-1}, $K_L = 0.12$ L mg^{-1} ($R^2 = 0.98$), and Freundlich $K_F = 12.5$, $1/n = 0.45$ ($R^2 = 0.96$), indicating monolayer dominance with heterogeneity.

3.8.9. TOC and COD removal efficiency. Mineralization of malachite green during photocatalysis was quantitatively tracked by both total organic carbon (TOC) and chemical oxygen demand (COD) analyses. TOC measurements showed a 60% reduction of organic carbon after 90 minutes, indicating effective mineralization beyond dye decolorization. Complementary COD removal reached 68% over the same period, supporting extensive organic contaminant oxidation. UV-Vis spectroscopy further confirmed the progressive disappearance of aromatic chromophores, consistent with mineralization (Fig. S5).

3.8.10. Efficacy of Ag-MOF against a range of organic contaminants. Pollutants were systematically investigated, and removal performance was found to be very dependent on the structure and complexity of the pollutant. In Fig. 12,

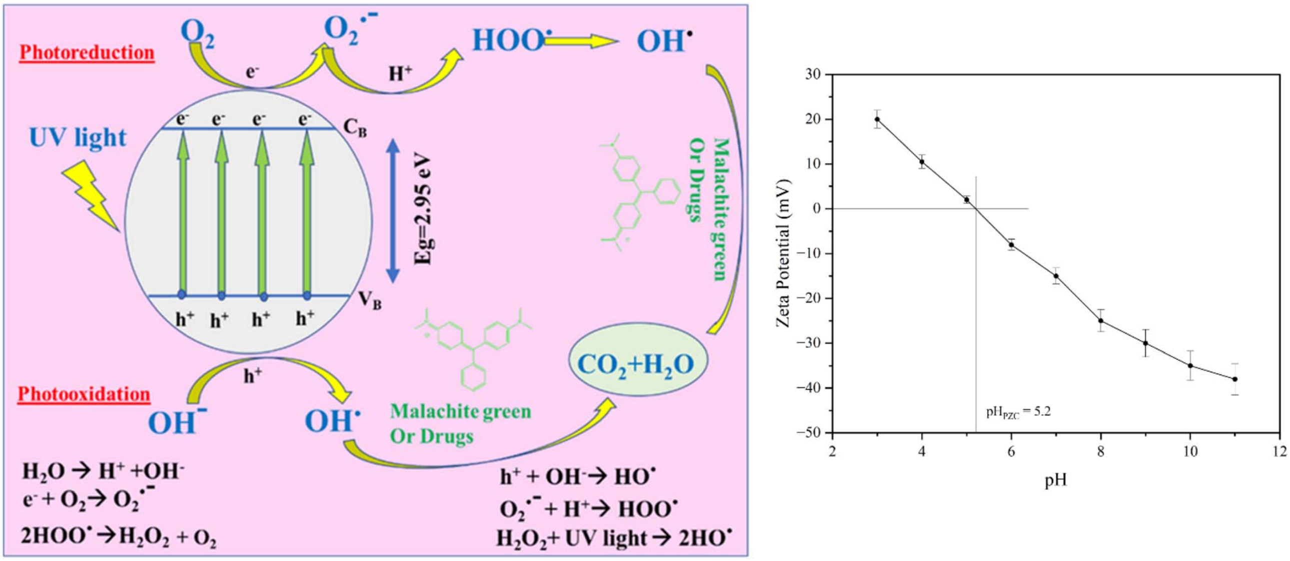

Fig. 11 Photocatalytic degradation mechanism for malachite green and the point of zero charge (pH_{pzc}) of the photocatalyst.

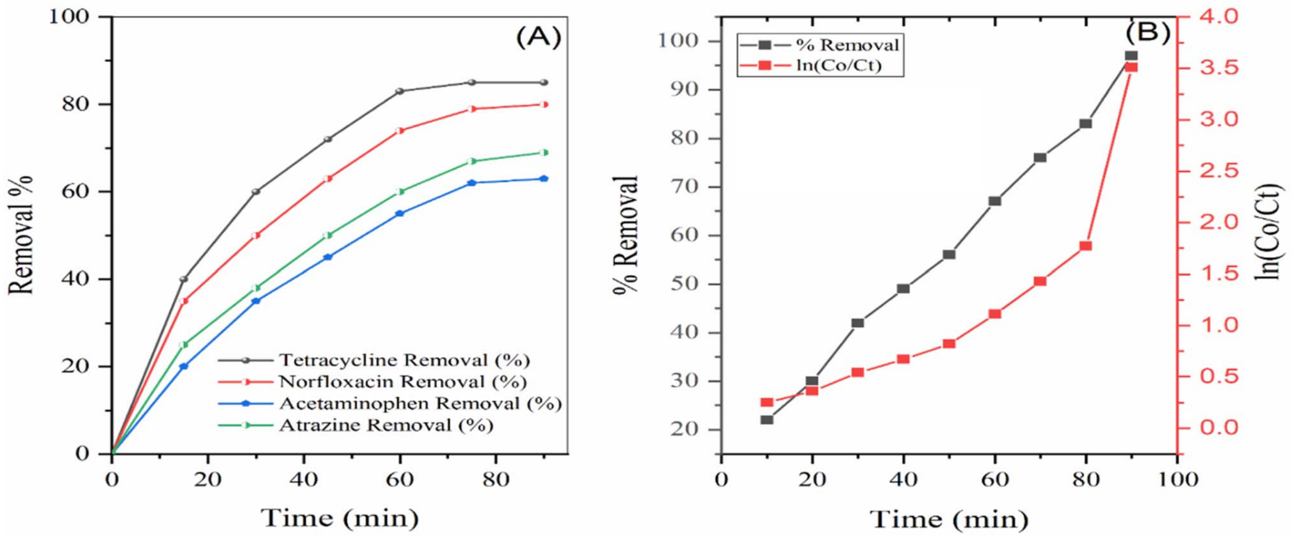

Fig. 12 (A) Photocatalytic degradation efficiencies of different pollutants over time using Ag-MOF catalyst, and (B) the pseudo-first-order kinetics of the photodegradation.

degradation rates (up to 85% and 80% for tetracycline and norfloxacin, respectively) were noted for the antibiotics, while acetaminophen and atrazine rates yielded moderate removal efficiencies (up to 63% and 70%, respectively). The time–course profiles were also informative in that they strongly illuminate the rapid initial reactivity of the Ag-MOF, with subsequent degradation rates plateauing at around 60–90 minutes; thus, the initial reactivity was fast, but the returns diminished as the substrate concentration decreased. For drug pollutants, the absorption peaks at characteristic wavelengths gradually diminish over time, indicating progressive disruption of their molecular structure and confirming the photocatalyst's ability to degrade pharmaceuticals as well (Fig. S6). The difference in removal efficiency for the classes of pollutants reinforces the conclusion that molecular stability and spanning functional groups influence the photocatalytic degradation under the conditions tested.

3.8.11. Ag-MOF sustainability and reusability. In subsequent photocatalytic degradation experiments, the Ag-MOF produced from the first cycle of the original photocatalytic degradation experiment was reapplied. The catalyst was repeatedly rinsed with 25 mL of ethanol and 25 mL of distilled water before being dried in a vacuum oven for one hour at 50 °C to make it suitable for reuse. Using identical experimental conditions to those used in the first cycle, the dried catalyst was subsequently applied in a second photocatalytic degradation experiment. Additionally, during the six cycles, the reusability of the particles was investigated. The fraction of MG dye that was

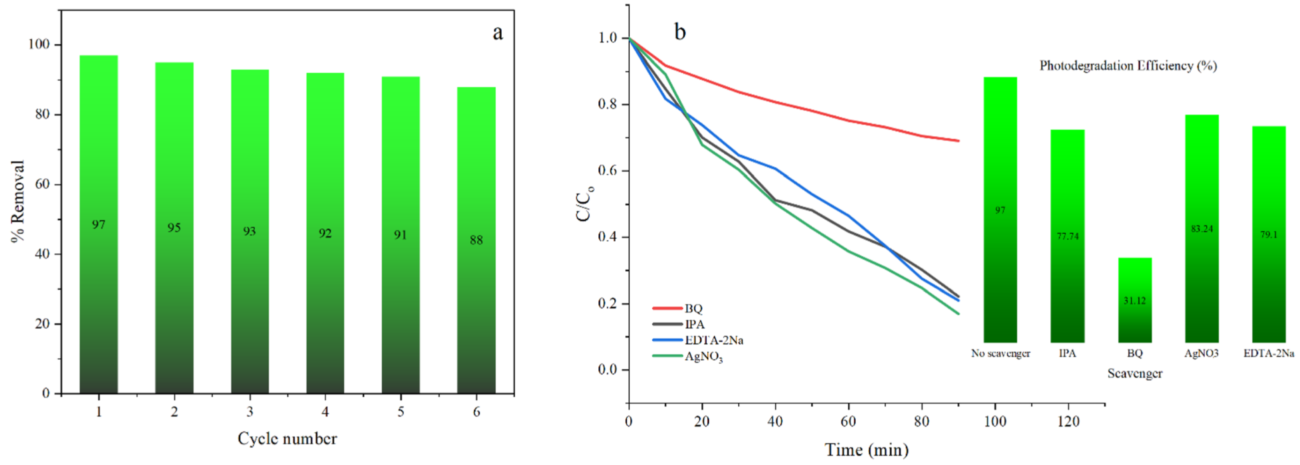

Fig. 13 (a) Reusability and sustainability of Ag-MOF, and (b) photocatalytic activities of the degradation of MG in the presence of various scavengers.

photocatalytically degraded using the Ag-MOF was plotted against the cycle number, as depicted in Fig. 13. Surprisingly, the data demonstrated very minimal changes in the percentage of dye decolorization during the six photocatalytic cycles. These remarkable findings indicate the efficacy of the proposed catalyst and its sustainability for repeated use with predictable dye degradation. Powder X-ray diffraction (PXRD) was used to assess changes in the structure of the catalyst post-reaction (Fig. S7), confirming that the crystallinity was unchanged (XRD peaks identical to those of fresh material), indicating no degradation from dye oxidation or ROS exposure.

A silver leaching test was carried out using AAS. After photocatalytic reactions, the mixture was centrifuged to remove Ag-MOF particulates, and the supernatant was carefully collected. The concentration of Ag^+ ions released into the solution was determined at the wavelength characteristic of silver (328.1 nm). After photocatalytic degradation of MG, the silver ion concentration in the solution was measured as 0.035 mg L^{-1} by AAS, corresponding to a total silver leaching of 0.0035 mg in 100 mL of solution; given that the initial silver content was approximately 0.097 mg, this represents a low leaching level of about 3.6%. This minimal silver release indicates that the Ag-MOF photocatalyst retains most of its silver during the reaction, demonstrating good structural stability and suitability for repeated use in water treatment applications.

3.8.12. Scavenger tests. To investigate the photocatalytic mechanism of the Ag-MOF, scavenger trapping experiments were conducted.[38,39] The MOF showed about 97% degradation of MG without scavengers. As shown in Fig. 13, addition of isopropanol (IPA; an $^{\bullet}OH$ scavenger) or EDTA-2Na (an h^+ scavenger) caused minimal changes, indicating a minor role for hydroxyl radicals and h^+. However, the addition of *p*-benzoquinone (BQ; an $O_2^{\bullet-}$ scavenger) significantly reduced the degradation efficiency to 31.12%. Thus, $O_2^{\bullet-}$ plays a dominant role in the degradation of MG.

Dose-dependent scavenging experiments were performed. For *p*-benzoquinone (BQ) trapping $O_2^{\bullet-}$, degradation efficiency fell steadily from 97% at 0 mM to 31% at 1 mM, showing strong inhibition (Table S3). In comparison, isopropanol (IPA), for $^{\bullet}OH$, had almost no effect, backing up its minor part. Hole (EDTA-2Na) and electron ($AgNO_3$) scavengers followed suit, with little effect, solidifying $O_2^{\bullet-}$ as the main driver in our Ag-MOF photocatalysis.

The semiconductor nature of Ag-MOF was inferred from its photocatalytic performance and structural characteristics, supporting its n-type behavior, which is consistent with Ag nanoparticle incorporation enhancing electron mobility and reducing recombination (PL emission). This aligns with the observed dominance of $O_2^{\bullet-}$ in scavenging tests, indicating a conduction band (CB) that is negative enough for O_2 reduction (−0.33 V *vs.* NHE), while the valence band (VB ∼ +2.6 V *vs.* NHE from DFT) limits strong $^{\bullet}OH$ generation.[40–42]

3.8.13. Comparison of photocatalytic degradation efficiency of malachite green dye. The Ag-MOF photocatalyst achieved 97% degradation of MG dye in 90 min under UV light at pH 8, using 0.15 g of catalyst. This performance is comparable to those of Ag-Mn oxide nanoparticles (99% in 60 min, sunlight) and Fe@(Alg-CMC) (98.8% in 30 min, UV-A light), and higher than that of Ag-ZnO nanofibers (93.5% in 60 min). These results highlight Ag-MOF as an effective material for MG dye removal (Table 1).

3.9. Synthesis of 7-hydroxy-4-methyl coumarin

According to the Ag-MOF catalytic activity data, various effects were investigated, including the dosage of Ag-MOF, the molar ratio of reactants using Ag-MOF, and the reusability and sustainability of Ag-MOF.

3.9.1. Ag-MOF dose. The yield % varied with the quantity of Ag-MOF, as seen in Fig. 14. By increasing the quantity of Ag-MOF catalyst from 0.05 to 0.2 g, the yield % achieved its maximum at 0.1 g. At higher catalyst quantities, the yield gradually dropped, which might be because the large amount of MOF interacted with the reactant, resulting in extra intermediates, leading to reduced yields.

Table 1 Degradation efficiency of the Ag-MOF photocatalyst and other photocatalysts

Photocatalyst	Degradation (%)	Time (min)	pH	Light source	Catalyst dose (g)	Ref.
N/Na/Fe-TiO_2	97.89	25.38	9.89	Visible light	0.11	43
Ag-Mn-oxide nanoparticles	99	60	10	Sunlight	0.0017	44
FVZ3	92	180	3	Visible light	1	45
Fe@(Alg-CMC)	98.8	30	4	UV-A light	0.1	46
Ag-modified ZnO-polymeric nanofibers	93.5	60	10	Xenon lamp 500 W	0.2	47
Pd/Ag/N-TiO_2	75	60		Visible light	0.05	48
ZIF-8/Ag/Ag_2S nanocomposite	98.6	20	8	Visible light	0.02	49
ZIF-8/Bi_2O_3/$Ag_6Si_2O_7$ composites	98.6	20	8	Visible light	0.02	8
Ag-MOF	97	90	8	UV- light	0.15	Our work

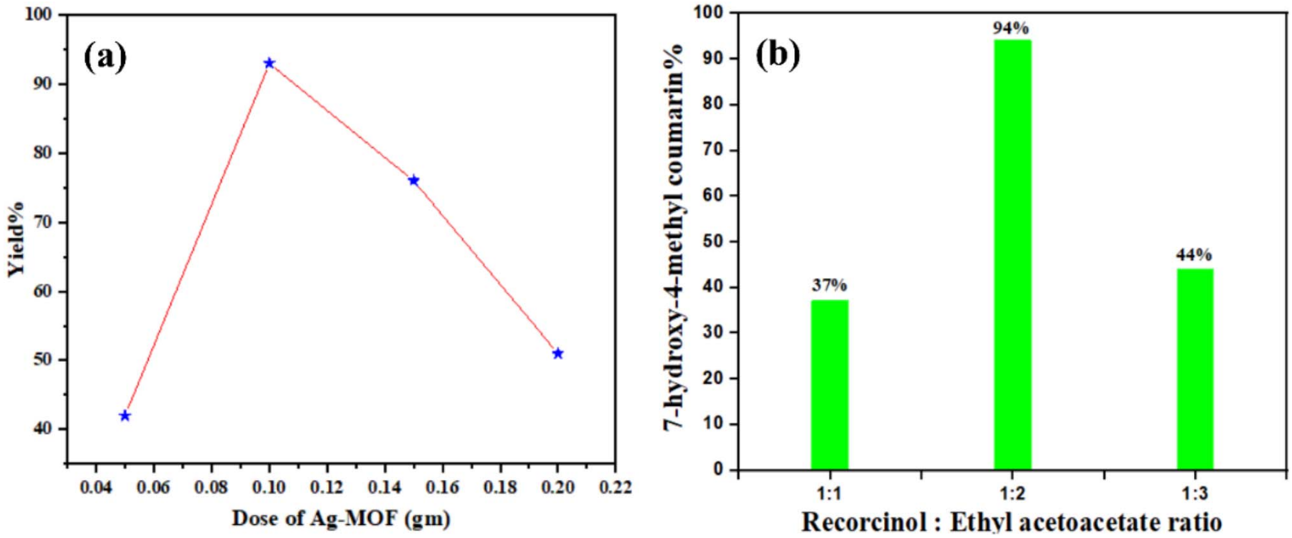

Fig. 14 (a) Effect of Ag-MOF dose and yield % of 7-hydroxy-4-methyl coumarin, and (b) the effect of the molar ratio of reactants on the yield of 7-hydroxy-4-methyl coumarin over Ag-MOF catalyst.

3.9.2. **Molar ratio of reactants using Ag-MOF.** As the molar ratio of resorcinol to ethyl acetoacetate was increased from 1 : 1 to 1 : 2, the coumarin yield increased from 37% to 94%, as shown in Fig. 14. When the ratio was adjusted to 1 : 3, the yield dropped to 44%. The catalyst effectiveness may have diminished as a result of ethyl acetoacetate saturation of the catalytic surface, which obstructed the acid sites.

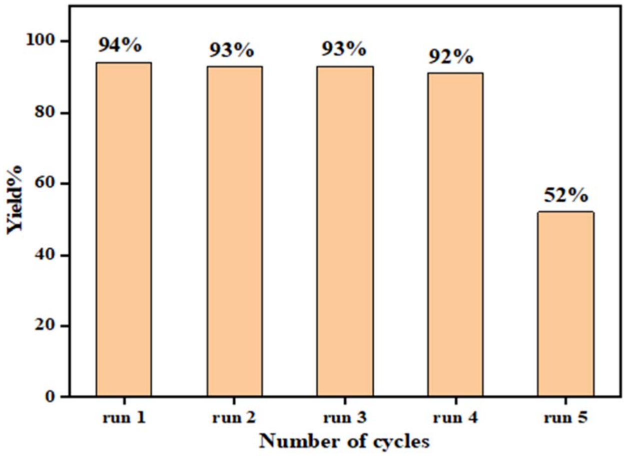

Fig. 15 Ag-MOF catalyst reusability shown by the yield of 7-hydroxy-4-methyl coumarin.

3.9.3. **Reusability and sustainability of Ag-MOF.** By filtering and then washing with ethyl acetate, Ag-MOF may be readily recovered from the reaction mixture after the catalytic reaction ends and utilized for the following cycle without activation. When the reusability of Ag-MOF was tested, it was determined that it could be reused at least five times. Fig. 15 indicates that the catalyst's activity declines from 94% to 52% after four applications because many of its surface-active sites are deactivated.

4. Conclusion

A silver-based metal–organic framework (Ag-MOF) was successfully synthesized *via* a green solvothermal method and comprehensively characterized by FT-IR, UV-Vis, XRD, SEM, EDX, TEM, and BET analyses. The Ag-MOF exhibited strong photocatalytic activity, achieving 97% degradation of malachite green dye under optimized conditions within 90 minutes. Surface acidity was quantified with a high density of acid sites

(4.16×10^{26} acid sites per g), contributing to the catalytic performance. TOC analysis confirmed significant mineralization during photocatalysis. Scavenger experiments confirmed superoxide radicals ($O_2^{\bullet -}$) as the primary active species responsible for the degradation process. Stability tests showed excellent reusability, retaining over 88% after six cycles. Collectively, these discoveries demonstrate the promise of Ag-MOF as a good photocatalyst for treating wastewater from the textile industry through photocatalytic processes.

Author contributions

Ahmed Hussain Jawhari: funding acquisition, project administration, conceptualization, supervision, software, and data curation. A. M. Ismael: software, methodology, writing – original draft preparation, visualization, formal analysis, and data curation.

Conflicts of interest

The authors declare that they have no known competing financial interests or personal relationships that could have appeared to influence the work reported in this paper.

Data availability

Data will be made available upon request.

Supplementary information (SI) is available. See DOI: **https://doi.org/10.1039/d5ra06391d**.

Acknowledgements

The authors gratefully acknowledge the funding of the Deanship of Graduate Studies and Scientific Research, Jazan University, Saudi Arabia, through project number: (RG24-S023).

References

1 R. Al-Tohamy, *et al.*, A critical review on the treatment of dye-containing wastewater: Ecotoxicological and health concerns of textile dyes and possible remediation approaches for environmental safety, *Ecotoxicol. Environ. Saf.*, 2022, **231**, 113160.

2 S. Dutta, *et al.*, Contamination of textile dyes in aquatic environment: Adverse impacts on aquatic ecosystem and human health, and its management using bioremediation, *J. Environ. Manage.*, 2024, **353**, 120103.

3 Z. Mohammadi, *et al.*, Interface engineering of a magnetic 2D-C3N4/Fe2O3/NiFe-LDH heterostructure for efficient photocatalytic degradation of methylene blue and rhodamine B dyes under visible light, *Appl. Clay Sci.*, 2023, **246**, 107182.

4 B. Lellis, *et al.*, Effects of textile dyes on health and the environment and bioremediation potential of living organisms, *Biotechnol. Res. Innov.*, 2019, **3**(2), 275–290.

5 R. Gopinathan, J. Kanhere and J. Banerjee, Effect of malachite green toxicity on non target soil organisms, *Chemosphere*, 2015, **120**, 637–644.

6 S. H. Abu-Hussien, *et al.*, Microbial Degradation, Spectral analysis and Toxicological Assessment of Malachite Green Dye by Streptomyces exfoliatus, *Molecules*, 2022, **27**(19), 6456.

7 S. A. Mustafa, A. J. Al-Rudainy and N. M. Salman, Effect of environmental pollutants on fish health: An overview, *Egypt. J. Aquat. Res.*, 2024, **50**(2), 225–233.

8 M. Khosravi-Far, *et al.*, ZIF-8/Bi2O3/Ag6Si2O7 nanocomposite as a novel sono-photocatalyst for the efficient degradation of malachite green, *Colloids Surf., A*, 2025, **726**, 137983.

9 K. Obaideen, *et al.*, The role of wastewater treatment in achieving sustainable development goals (SDGs) and sustainability guideline, *Energy Nexus*, 2022, **7**, 100112.

10 O. V. Obayomi, *et al.*, Exploring emerging water treatment technologies for the removal of microbial pathogens, *Curr. Res. Biotechnol.*, 2024, **8**, 100252.

11 L. Lin, H. Yang and X. Xu, Effects of Water Pollution on Human Health and Disease Heterogeneity: A Review, *Front. Environ. Sci.*, 2022, **10**, 880246.

12 H. Wang, X. Gao and Y. Zuo, Research and Application of Water Treatment Technologies for Emerging Contaminants (ECs): A Pathway to Solving Water Environment Challenges, *Water*, 2024, **16**, 1837.

13 A. El Golli, S. Contreras and C. Dridi, Bio-synthesized ZnO nanoparticles and sunlight-driven photocatalysis for environmentally-friendly and sustainable route of synthetic petroleum refinery wastewater treatment, *Sci. Rep.*, 2023, **13**(1), 20809.

14 A. Rafiq, *et al.*, Photocatalytic degradation of dyes using semiconductor photocatalysts to clean industrial water pollution, *J. Ind. Eng. Chem.*, 2021, **97**, 111–128.

15 W. Liu, *et al.*, Photocatalytic elimination of environmental pollutants by immobilized g-C3N4-based materials, *Surf. Interfaces*, 2025, **58**, 105846.

16 M. N. Abonyi, C. C. Obi and J. T. Nwabanne, Degradation of organic pollutants in wastewater using MOF-based catalysts: A review, *Next Mater.*, 2025, **8**, 100696.

17 S. Singh, *et al.*, Metal organic frameworks for wastewater treatment, renewable energy and circular economy contributions, *npj Clean Water*, 2024, **7**(1), 124.

18 S. Naghdi, *et al.*, Recent advances in application of metal-organic frameworks (MOFs) as adsorbent and catalyst in removal of persistent organic pollutants (POPs), *J. Hazard. Mater.*, 2023, **442**, 130127.

19 U. Farwa, *et al.*, Revolutionizing environmental cleanup: the evolution of MOFs as catalysts for pollution remediation, *RSC Adv.*, 2024, **14**(50), 37164–37195.

20 S. A. Moosaviyan, *et al.*, Photocatalytic decomposition of methylene blue and rhodamine B using Ag–Ag2SeO3/Ppy nano-photocatalyst from aqueous solutions: experimental design optimization, *J. Nanostruct. Chem.*, 2023, **14**, 6.

21 X. Chen, *et al.*, Photocatalytic Performance of the MOF-Coating Layer on SPR-Excited Ag Nanowires, *ACS Omega*, 2021, **6**(4), 2882–2889.

22 M. S. Khan, *et al.*, A review of metal–organic framework (MOF) materials as an effective photocatalyst for degradation of organic pollutants, *Nanoscale Adv.*, 2023, **5**(23), 6318–6348.

23 V. Shukla, *et al.*, Ag@Zn-MOF Composites: A Dual Function Material for Luminescent Detection, Dose Reliant Photodegradation of Ethion Insecticide and Enhanced Bioactivity, *Appl. Organomet. Chem.*, 2025, **39**(9), e70339.

24 Y. Sneha, *et al.*, Multifunctional metal (Ag, Bi)-organic frameworks: a versatile platform for photocatalytic degradation, CO2 and N2 reduction, and enhanced antibacterial applications, *Mater. Today Sustainability*, 2023, **24**, 100527.

25 J. R. Blanton, R. J. Papoular and D. Louër, PreDICT: a graphical user interface to the DICVOL14 indexing software program for powder diffraction data, *Powder Diffr.*, 2019, **34**(3), 233–241.

26 T. Lu and F. Chen, Multiwfn: A multifunctional wavefunction analyzer, *J. Comput. Chem.*, 2012, **33**(5), 580–592.

27 R. Dennington, T. A. Keith, and J. M. Millam, *GaussView, version 6.0. 16*, Semichem Inc., Shawnee Mission KS, 2016, vol. 13.

28 M. Frisch, *Gaussian 09, Revision D.01*, Gaussian Inc., Wallingford CT, 2009, vol. 201.

29 G. E. Said, *et al.*, Solvothermal Synthesis of Innovative and Efficient Ag/NA-MOF Nanoparticles for One-Pot Synthesis of Imidazoquinazolinones and In vitro Validation as Anti-Alzheimer Agents, *J. Organomet. Chem.*, 2025, **1032**, 123623.

30 M. Opanasenko, M. Shamzhy and J. Čejka, Solid Acid Catalysts for Coumarin Synthesis by the Pechmann Reaction: MOFs versus Zeolites, *ChemCatChem*, 2013, **5**(4), 1024–1031.

31 D. Wahyuningrum, M. Zulqarnaen and V. Suendo, The synthesis and characterization of 7-hydroxy-4-methylcoumarin and the investigation of the fluorescence properties of its 7-hydroxy-4-methylcoumarin-chitosan films, *AIP Conf. Proc.*, 2014, **1589**(1), 169–173.

32 Y. Zhang, *et al.*, Cholinium ionic liquids as cheap and reusable catalysts for the synthesis of coumarins via Pechmann reaction under solvent-free conditions, *RSC Adv.*, 2014, **4**(44), 22946–22950.

33 P. Makuła, M. Pacia and W. Macyk, How To Correctly Determine the Band Gap Energy of Modified Semiconductor Photocatalysts Based on UV–Vis Spectra, *J. Phys. Chem. Lett.*, 2018, **9**(23), 6814–6817.

34 A. Ejsmont, A. Jankowska and J. Goscianska, Insight into the Photocatalytic Activity of Cobalt-Based Metal–Organic Frameworks and Their Composites, *Catalysts*, 2022, **12**(2), 110.

35 S. A. El-Hakam, *et al.*, Synthesis of sulfamic acid supported on Cr-MIL-101 as a heterogeneous acid catalyst and efficient adsorbent for methyl orange dye, *RSC Adv.*, 2018, **8**(37), 20517–20533.

36 M. Heidari Nezhad Janjanpour, *et al.*, Study of the Ionization Potential, Electron Affinity and HOMO-LUMO Gaps in the Smal Fullerene Nanostructures, *Chem. Rev. Lett.*, 2018, **1**(2), 45–48.

37 A. M. Younis, *et al.*, Iron(III), copper(II), cadmium(II), and mercury(II) complexes of isatin carbohydrazone Schiff base ligand (H3L): Synthesis, characterization, X-ray diffraction, cyclic voltammetry, fluorescence, density functional theory, biological activity, and molecular docking studies, *Appl. Organomet. Chem.*, 2021, **35**(7), e6250.

38 A. M. Younis, *et al.*, Synthesis and Assessment of Novel Co-AAP-MOF as a Highly Effective and Reusable Photocatalyst for the Degradation of Organic Pollutants, *J. Inorg. Organomet. Polym. Mater.*, 2025, **35**, 8552–8566.

39 T. Tan, D. Beydoun and R. Amal, Effects of organic hole scavengers on the photocatalytic reduction of selenium anions, *J. Photochem. Photobiol., A*, 2003, **159**(3), 273–280.

40 S. Navalón, *et al.*, Metal–Organic Frameworks as Photocatalysts for Solar-Driven Overall Water Splitting, *Chem. Rev.*, 2023, **123**(1), 445–490.

41 K. Gelderman, L. Lee and S. W. Donne, Flat-Band Potential of a Semiconductor: Using the Mott–Schottky Equation, *J. Chem. Educ.*, 2007, **84**(4), 685.

42 W. Lu, *et al.*, Ag Nanoparticles-decorated p-type CuO/n-type ZnO heterojunction nanofibers with enhanced photocatalytic activities for dye degradation and disinfection, *J. Alloys Compd.*, 2023, **968**, 171864.

43 A. T. Amigun, *et al.*, Photocatalytic degradation of malachite green dye using nitrogen/sodium/iron-TiO2 nanocatalysts, *Results Chem.*, 2022, **4**, 100480.

44 Z. Xu, *et al.*, Enhanced Photocatalytic Degradation of Malachite Green Dye Using Silver–Manganese Oxide Nanoparticles, *Molecules*, 2023, **28**, 6241.

45 E. M. Mostafa and E. Amdeha, Enhanced photocatalytic degradation of malachite green dye by highly stable visible-light-responsive Fe-based tri-composite photocatalysts, *Environ. Sci. Pollut. Res.*, 2022, **29**(46), 69861–69874.

46 D. Karadeniz, N. Kahya and F. B. Erim, Effective photocatalytic degradation of malachite green dye by Fe(III)-Cross-linked Alginate-Carboxymethyl cellulose composites, *J. Photochem. Photobiol., A*, 2022, **428**, 113867.

47 M. F. Elkady and S. H, Hassan Photocatalytic Degradation of Malachite Green Dye from Aqueous Solution Using Environmentally Compatible Ag/ZnO Polymeric Nanofibers, *Polymers*, 2021, **13**, 2033.

48 N. Chauhan, *et al.*, Synthesis of nitrogen & palladium co-doped mesoporous titanium dioxide nanoparticles via evaporation induced self assembly method and study of their photocatalytic properties, *J. Mol. Struct.*, 2019, **1185**, 219–228.

49 M. Khosravi-Far, *et al.*, Efficient photocatalytic degradation of malachite green dye from wastewater using facilely synthesized ternary ZIF-8/Ag/Ag2S nanocomposite: Optimization by RSM (CCD), *Process Saf. Environ. Prot.*, 2024, **190**, 46–62.